

PCCP

Accepted Manuscript



This is an *Accepted Manuscript*, which has been through the Royal Society of Chemistry peer review process and has been accepted for publication.

Accepted Manuscripts are published online shortly after acceptance, before technical editing, formatting and proof reading. Using this free service, authors can make their results available to the community, in citable form, before we publish the edited article. We will replace this *Accepted Manuscript* with the edited and formatted *Advance Article* as soon as it is available.

You can find more information about *Accepted Manuscripts* in the [Information for Authors](#).

Please note that technical editing may introduce minor changes to the text and/or graphics, which may alter content. The journal's standard [Terms & Conditions](#) and the [Ethical guidelines](#) still apply. In no event shall the Royal Society of Chemistry be held responsible for any errors or omissions in this *Accepted Manuscript* or any consequences arising from the use of any information it contains.

Cite this: DOI: 10.1039/c0xx00000x

www.rsc.org/xxxxxx

ARTICLE TYPE

Origin of photoactivity in graphitic carbon nitride and strategies for enhancement of photocatalytic efficiency: Insights from first-principles computations.

Haijun Zhang,^a Xueqin Zuo,^a Huaibao Tang,^a Guang Li,^{a,*} and Zhen Zhou^{b,*}

⁵ Received (in XXX, XXX) Xth XXXXXXXXX 20XX, Accepted Xth XXXXXXXXX 20XX
DOI: 10.1039/b000000x

The origin of the photoactivity in graphitic carbon nitride (g-C₃N₄) and the strategies for improving its photocatalytic efficiency were systematically investigated through first-principles computations. We found that g-C₃N₄ composed of tri-*s*-triazine units (g-CN1) is preferable in photocatalysis, owing to its visible-light absorption and appropriate band edge potentials. Despite the benefit from nanocrystallization of g-CN1, excessively minimized and passivated g-CN1 nanosheets (g-CN1NSs) should be inhibited, due to the intensely broadened band gaps in these structures. C- or N-vacancies in g-CN1NSs lead to gap states and smaller band widths, which should also be restrained. Compared with C substitution in B doped g-CN1NSs, N-substitution is favourable for enhancing the photoactivity of g-CN1NSs, due to the red-shift light absorption and absent gap states within this structure. Both WTe₂ coupled and CdSe cluster loaded g-CN1NSs have decreased band gaps and directly separated carriers, which is beneficial to promote the photoactivity of g-CN1NSs. Among these modified g-CN1NSs photocatalysts, WTe₂ coupled g-CN1NS is more preferable, resulting from its smaller band gap, free gap states and more rapid migration of excitons.

1. Introduction

Among the wide variety of green earth and renewable energy projects under way, semiconductor photocatalysis has become one of the most potential technologies because it facilitates the utilization of energy from natural sunlight or artificial indoor illumination. Numerous attempts have focused on the semiconductor photocatalysts for degradation of organic pollutants, hydrogen production from water and photocatalytic reduction of CO₂. In terms of energy conversion and commercial application, the efficiency of visible-light absorption becomes one of the key factors that determine the performance of solar cell absorber and photocatalytic materials, because nearly 50% of solar energy comes from the visible-light part.

Recently, a polymeric semiconductor on basis of graphitic carbon nitride (g-C₃N₄) has proved a promising photocatalyst,¹⁻⁶ due to its abundance, high stability and visible-light absorption. There are two types of g-C₃N₄ structural isomers, which consist of *s*-triazine units (ring of C₃N₃) or tri-*s*-triazine units (tri-ring of C₆N₇), respectively. For simplicity, the bulk g-C₃N₄ consists of tri-*s*-triazine units and *s*-triazine units were labeled as g-CN1 and g-CN2 in this work, respectively. As an analogue of graphite, bulk g-C₃N₄ is a layered solid with *ABA* stacking of hexagonal planes of carbon and nitrogen atoms, which leads to anisotropy in chemical bonding and quasi-two-dimensional structure of g-C₃N₄ (as shown in Fig. 1). Encouraged by the easy exfoliation of graphite into monolayer or few-layer graphene on large scale, it is

possible to obtain g-C₃N₄ nanosheets from bulk g-C₃N₄ when one considers the weak van der Waals interaction between layers in g-C₃N₄.⁴ Compared with traditional bulk materials, two-dimensional (2D) atomic crystals have intrinsic advantages as photocatalytic materials, due to their limited thickness and large surface.⁵⁻⁹

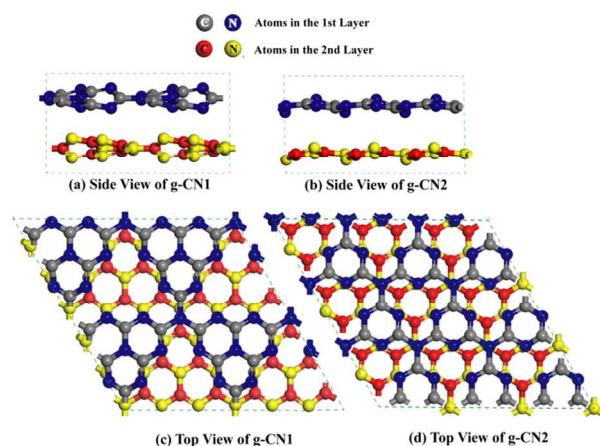


Fig. 1 Geometric structures of g-CN1 and g-CN2.

It is reported that pure g-C₃N₄ presents a band gap of 2.7 eV,¹ corresponding to absorption of blue light up to 450 nm, which is not sufficient enough for solar harvesting. To get better performance of g-C₃N₄ photocatalysts, many experimental and computational investigations have focused on the enhancement of

its visible-light absorption. Conventional strategies, including chemical doping,¹⁰⁻¹³ quantum dot loading,¹⁴⁻¹⁷ dye sensitizing,¹⁸ semiconductor coupling,¹⁹⁻²⁶ and morphology controlling,²⁷⁻³⁰ have been used for tuning the electronic structure of g-C₃N₄ photocatalysts and many good results have been achieved. However, the optical absorption spectrum is not the only factor that determines the efficiency of photocatalysts. After the light with a certain wavelength falls onto a semiconductor, electrons will be excited to the conduction band of semiconductors, and holes will be left in the valence band. These excitons will then rapidly migrate to the surface of photocatalysts and undergo subsequent oxidation and reduction reactions with molecules or groups absorbed on the surface of semiconductors. In the meantime, the electron in the conduction band minimum (CBM) will continually recombine with the hole in the valence band maximum (VBM), which should be suppressed in photocatalysis. Moreover, the ability of a material to perform redox reactions at its surface depends on the position of its band edges relative to the free energy of the reactions of interest. The reactions are thermodynamically favourable if their free energies are located within the band gap region, namely, the VBM (or CBM) levels are lower (or higher) than the free energies, E_{ox} (or E_{red}), of oxidation (or reduction) reactions. We also need to consider that narrowing the band gaps and tuning the band edge potentials have competitive effects on the photoactivity of semiconductors. Narrowing the band gap, accompanied by the increase of the VBM or the decrease of the CBM, may cause the diminishing energy difference between VBM (CBM) levels and E_{ox} (or E_{red}). Therefore, other electronic properties, including charge mobility, carrier separation, and redox potential of band edges, are also significant and need to be investigated and compared in the studies of photocatalysis. However, these complex factors have not been entirely considered and analyzed in most recent reports on g-C₃N₄ photocatalysts.

In this work, considering various influences, we have computationally investigated the origin of photocatalytic activation of pure and defective g-C₃N₄ and compared some conventional strategies for the improvement of its efficiency. Our aim was to select and further optimize the ideal method of enhancing the performance of g-C₃N₄ photocatalysts. Moreover, because the standard density functional theory (DFT) method cannot predict the excited states and underestimates the band gaps of semiconductors, we used the recently developed Heyd-Scuseria-Ernzerhof (HSE) functional in this work. In view of the computational burden of hybrid DFT method, the standard DFT was also employed for optimizing the models with hundreds of atoms after benchmark.

2. Computational Details

Our first-principles computations were performed by using plane wave (PAW)^{31,32} method as implemented in the Vienna ab initio simulation package (VASP).³³ Electronic exchange and correlation effects were treated by using the generalized gradient approximation (GGA) with Perdew-Burke-Ernzerhof (PBE) parametrization.³⁴ For greater accuracy of the electronic and optical properties, Heyd-Scuseria-Ernzerhof (HSE06)³⁵ hybrid functional was also employed. The screening parameter μ in HSE was fixed at 0.2 Å⁻¹ and the mixing parameter α was set as 0.25.³⁶

A 500 eV cutoff for the plane-wave basis set was adopted in all computations. The convergence criteria for energy and force were 10⁻⁴ eV and 10⁻³ eV·Å⁻¹, respectively. The Brillouin zone was represented by Gamma-centered unit cells with 7×7×7 Monkhorst-Pack k-point mesh for geometry optimization of bulk g-C₃N₄. A damped van der Waals correction based on Grimme's scheme³⁷ is also incorporated to better describe the nonbonding interaction between the atomic layers within g-C₃N₄ crystals. Band structures of bulk g-CN1 were computed along the special lines connecting the following high-symmetry points: G (0, 0, 0), Z (0, 0, 0.5), T (0.5, 0, 0.5), Y (0.5, 0, 0), S (0.5, 0.5, 0), X (0, 0.5, 0), U (0, 0.5, 0.5), and R (0.5, 0.5, 0.5) in the k-space. While the band structures of bulk g-CN2 were computed along G (0, 0, 0), Z (0, 0, 0.5), L (0, 0.5, 0.5), M (0, 0.5, 0), N (0.5, 0.5, 0), W (0.5, 0, 0), K (0.5, 0, 0.5), and V (0.5, 0.5, 0.5) in the k-space.

In search of the preferred stacking geometry, we computed the total energies of several possible structures with different relative shifts between *A* and *B* planes. We found that the *ABA*-stacking geometry of g-CN1 or g-CN2, as shown in Figure 1, have the lowest energy among these investigated structures. Meanwhile, the configurations with *C*-against-*C* and *N*-against-*N* geometries (*AA* stacking) have total energies larger than that of the preferred configuration (*ABA* stacking) by 0.3~0.6 eV per unit cell. Therefore, we only investigated the g-CN1 and g-CN2 with *ABA* stacking structures, which are energetically favourable, to simplify the computations and reduce the computational burden.

To investigate the optical properties of g-C₃N₄ crystals, the frequency-dependent dielectric matrix is also calculated by using the HSE06 functional and expanding over a 10×10×10 k-point mesh. The complex dielectric constants at a given frequency can be defined as $\varepsilon(\omega) = \varepsilon_1(\omega) + i\varepsilon_2(\omega)$. The expression for the absorption coefficient $I(\omega)$ was given as:³⁸

$$I(\omega) = \sqrt{2\omega}[\sqrt{\varepsilon_1(\omega)^2 + \varepsilon_2(\omega)^2} - \varepsilon_1(\omega)]^{1/2} \quad (1)$$

According to the equation, we can obtain the light absorbing information from the value of imaginary part. Only if the imaginary part $\varepsilon_2(\omega) > 0$, the absorption coefficient was above zero. The imaginary part is determined by a summation over empty states using the equation³⁹

$$\varepsilon_{\alpha\beta}^{(2)}(\omega) = \frac{4\pi^2 e^2}{\Omega} \lim_{q \rightarrow 0} \frac{1}{q^2} \sum_{c,v,\bar{k}} 2W_{\bar{k}} \delta(\varepsilon_{c\bar{k}} - \varepsilon_{v\bar{k}} - \omega) \times \left\langle u_{c\bar{k}+e_a\bar{q}} \middle| u_{v\bar{k}} \right\rangle \left\langle u_{c\bar{k}+e_b\bar{q}} \middle| u_{v\bar{k}} \right\rangle^* \quad (2)$$

where the indices *c* and *v* represent conduction and valence band states, respectively, and $u_{c\bar{k}}$ is the cell periodic part of the orbitals at the *k* point. A large number of empty conduction band states (almost twice more than the number of valence band) are included for the summation of equation (2).

As mentioned in the introduction, the band edge alignment of the CBM and VBM relative to the water redox potential determines whether a semiconductor can be used as a photoanode or photocathode. As presented in other reports,^{40,41} the water reduction potential $\phi(\text{H}^+/\text{H}_2)$ at pH = 0 is defined as the zero potential, known as the normal hydrogen electrode (NHE) potential, and all other potentials are referenced to this NHE. For

instance, the water oxidation potential is usually said to be 1.23 V relative to NHE and $1.23 \text{ V} = \phi(\text{O}_2/\text{H}_2\text{O}) - \phi(\text{H}^+/\text{H}_2)$. When the band edge position of a semiconductor *A* has not been measured experimentally, it can be also estimated theoretically. One method is based on the calculated band offsets between the semiconductor *A* and another semiconductor *B* whose band edge position relative to NHE is known. Then the band edge position of *A* relative to NHE can be derived.⁴⁰ Following the same procedure, we performed computations to obtain the natural valence band offset of two compounds at their respective equilibrium positions using the description⁴²⁻⁴⁴

$$\Delta E_v(A/B) = \Delta E_{v,c}(B) - \Delta E_{v,c}(A) + \Delta E_{c,c}(A/B) \quad (3)$$

Here $\Delta E_{v,c}(A) = E_v(A) - E_c(A)$ [the same for $\Delta E_{v,c}(B)$] is the energy difference between the VBM and core level at the equilibrium lattice constant and $\Delta E_{c,c}(A/B) = E_c(B) - E_c(A)$ is the core level energy difference between the two core levels in a relaxed (*A/B*) heterostructure, where a common energy reference exists. The validity of the above approach is based on the assumption that the reference levels have zero absolute deformation potential and thus align between the bulk and heterostructures, which is justified when compounds *A* and *B* are lattice matched. In the above view, we selected hexagonal WTe_2 and CdTe crystal, which match $\text{g-C}_3\text{N}_4$ lattice well and have known band edge positions relative to NHE,⁴⁵ to form heterostructure with g-CN1 and g-CN2 , respectively, for the band alignment calculations.

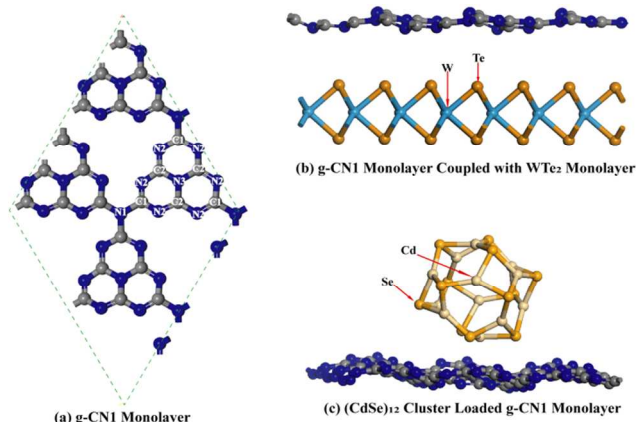


Fig. 2 Geometry structures of (a) g-CN1 , (b) g-CN2 and (c,d) modified g-CN1 monolayers.

In view of the well-matched crystal lattices of the WTe_2 and g-CN1 monolayer, the wurtzite WTe_2 monolayer was used to couple with the g-CN1 monolayer for further enhancement of $\text{g-C}_3\text{N}_4$ (see Fig. 2b). In addition, the quantum dot sensitized g-CN1 , namely CdSe-g-CN1 heterostructured photocatalysts, consists of the frequently-used CdSe quantum dots and g-CN1 monolayer. The CdSe cluster used in our computations was composed of 12 Cd and 12 Se atoms.^{46,47} After construction of the $(\text{CdSe})_{12}$ cage-structure cluster, it was optimized at the G point and relaxed to the minimum energy (as shown in Fig. 2c). For a g-CN1 monolayer, due to the different chemical environments, nitrogen atoms are separated into three kinds, namely, N1 , N2 and N3 , while carbon atoms are differentiated into C1 and C2 (as shown in Fig. 2a). The computations of 2D systems, including $\text{g-C}_3\text{N}_4$

nanosheets, $\text{WTe}_2\text{-g-CN1}$ and CdSe-g-CN1 heterostructures, as well as pure and modified g-CN1 monolayer, were performed by using the slab model, in which a finite number of crystal layers in a three-dimensional periodic cell via introduction of a vacuum gap in the third dimension (*Z*). The vacuum space is set as 17 Å, which is large enough to separate the interaction between periodic images. A $7 \times 7 \times 1$ k-point grid and a cutoff energy of 500 eV were used in the relaxation of 2D structures. All the band structures of 2D systems were computed along the following high-symmetry points: G (0, 0, 0), M (0.5, 0.5, 0), X (0, 0.5, 0), and G (0, 0, 0) in the k-space.

3. Results and Discussion

3.1 Geometric, Electronic and Optical Properties of bulk $\text{g-C}_3\text{N}_4$

In the case of introducing weak van der Waals interaction, we found that both the $\text{g-C}_3\text{N}_4$ bulk and nanosheets have the most stable geometry in a buckled configuration, as suggested in Deifallah et al.'s report.⁴⁸ Under periodic boundary conditions, the buckling distortion of the C-N layers is expressed as a wavelike conformation of the sheets (as shown in Fig. 1a,b). Despite up and down motion of the C or N atoms in the C-N layers, basic construction units of g-CN1 and g-CN2 are still tri-*s*-triazine and tri-*s*-triazine, respectively. The calculated lattice constants of bulk g-CN1 are $a = 6.99 \text{ \AA}$ and $c = 6.56 \text{ \AA}$, which agree well with the lattice constants from the XRD patterns reported by Wang et al ($a = 6.81 \text{ \AA}$, $c = 6.52 \text{ \AA}$).¹ While the lattice constants of bulk g-CN2 are $a = 4.72 \text{ \AA}$ and $c = 6.64 \text{ \AA}$ in our computations, which are also accordant with the experimental study ($a = 4.70 \text{ \AA}$, $c = 6.34 \text{ \AA}$).⁴⁹ It is proposed that the weak van der Waals interaction between layers could not be ignored in computational studies. As the result of this weak interaction, the $\text{g-C}_3\text{N}_4$ bulk can be easily stripped to get a large surface area, which is beneficial to the photocatalytic reaction.

Through HSE06 Method, we computed the band structures (Fig. 3) and optical properties (Fig. 4) of the bulk $\text{g-C}_3\text{N}_4$. We can see from Fig. 3a that g-CN1 has an indirect band gap of 2.71 eV, which is in accordance with the experimental reports.¹ The CBM of g-CN1 appears at the Y point, while the VBM of it is located at one point within the YS line. As shown in Fig. 3b, both the CBM and VBM of g-CN2 are located at the G point. The computed band gap of g-CN2 is 3.3 eV, which is a little larger than the experimental results (3.1 eV)⁵⁰ and the computed E_g by Reshak et al (3.0 eV).⁵¹ Note that, Reshak et al have systematically compared several DFT functionals for computing the band structures of g-CN2 . As expected, the standard DFT method, such as the LDA and GGA approaches, always underestimate the band gaps of semiconductors. They suggested that band gaps of semiconductors can be accurately predicted by the recently developed modified Becke-Johnson (mBJ) functionals. Significantly, our HSE06 can also estimate exact value of the band gaps of graphitic carbon nitrides, which are approaching to the experimental band gaps.

It is supposed that indirect band gaps of photocatalysts may be more favourable than direct ones for retarding the recombination of photo-induced carriers, due to the different momentums of two positions in the k-space. According to the band gaps of these two kinds of $\text{g-C}_3\text{N}_4$, g-CN1 has the visible-light response but g-CN2

can not absorb visible light. To further confirm their absorption properties, we calculated the complex dielectric constants $\varepsilon(\omega) = \varepsilon_1(\omega) + i\varepsilon_2(\omega)$, and represented the imaginary part $\varepsilon_2(\omega)$ in Fig. 4. The $\varepsilon_2(\omega)$ term of the bulk g-C₃N₄ consist of $\varepsilon_{xy}(\omega)$ and $\varepsilon_{zz}(\omega)$, which are the components perpendicular and parallel to the z direction, respectively. As shown in Fig. 4a, the bulk g-CN1 has obvious absorption peaks at 2.81 eV and 2.92 eV, resulting in the visible-light absorption of these materials. Nevertheless, the g-CN2 has absorption peaks higher than 3.2 eV and thus can only absorb the ultraviolet (UV) light.

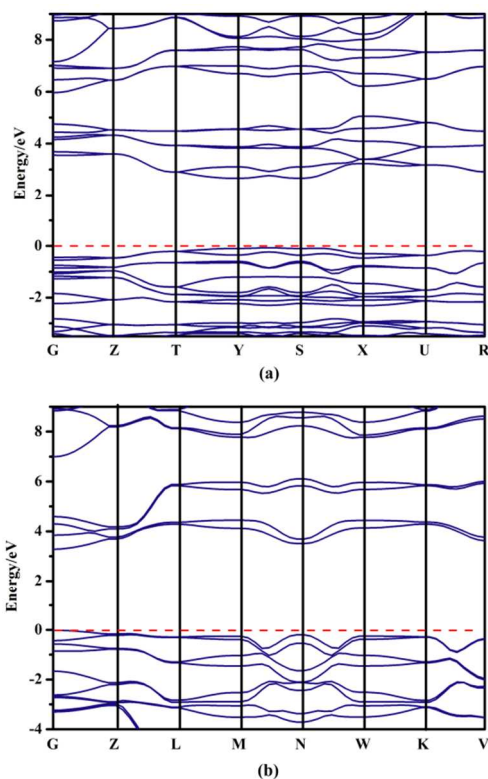


Fig. 3 Band structures of bulk (a) g-CN1 and (b) g-CN2, computed by HSE06. Red dashed lines represent the Fermi level at 0 eV.

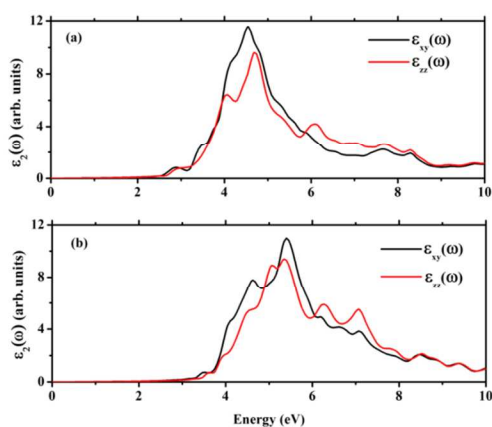


Fig. 4 Imaginary parts of dielectric constants for bulk (a) g-CN1 and (b) g-CN2.

As noted above, the band edge potential of photocatalysts is another predominate factor that determines their performance in

photocatalytic water-splitting. As shown in Fig. 5, the g-CN1 covalent solid possesses a band gap of 2.7 eV, with suitable positions of CBM and VBM ($E_{\text{CBM}} = -0.73$ V and $E_{\text{VBM}} = 1.97$ V vs NHE, pH = 0), which is in agreement with the results of Ma et al.'s computations¹² and approaches experimental results.² All three semiconductors, represented in Fig. 5, are capable of running a set of relevant activation reactions, such as direct reduction of carbon dioxide to methane, activation of O₂ to O_2^- and mineralization of organic dyes to CO₂. As is known, only if the difference between CBM and water reduction potential $[\phi(\text{H}^+/\text{H}_2)]$ is large enough, H⁺ should accept the photo-excited electrons from semiconductors. With enough difference between the VBM and water oxidation potential $[\phi(\text{O}_2/\text{H}_2\text{O})]$, the semiconductors should also accept electrons from OH⁻. Obviously, g-CN1 was also able to split water with simultaneous evolution of hydrogen and oxygen in the presence of electron donors and acceptors. While g-CN2 only donates electrons to H⁺ but does not accept electrons from OH⁻. As the result of UV light absorption and unsuitable band edge positions, the g-CN2 photocatalysts are ill-suited for hydrogen evolution from water-splitting. Despite more negative E_{CBM} (vs. NHE) than $\phi(\text{H}^+/\text{H}_2)$, TiO₂ is not recommended for photocatalytic water-splitting, due to its UV light absorption and the tiny difference between $\phi(\text{H}^+/\text{H}_2)$ and E_{CBM} of TiO₂.

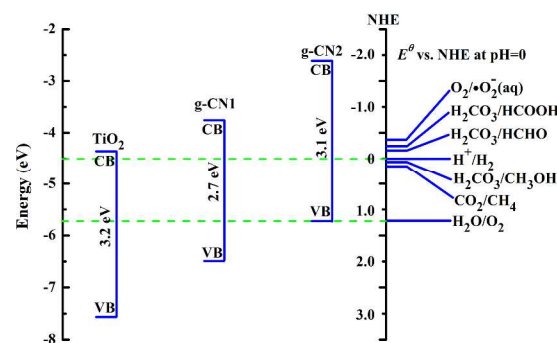


Fig. 5 Band-edge positions of g-CN1 and g-CN2 photocatalysts relative to the energy levels of varied redox couples in water at pH = 0. As a reference, band-edge positions of titanium dioxide are also given.

In view of the above-mentioned facts, g-CN1 has visible-light absorption, appropriate band-edge positions and indirect band gap for hindering the recombination of photo-excited e⁻-h⁺ pairs. Consequently, the g-CN1 photocatalysts are more favourable for hydrogen production through photochemical water-splitting. Maybe it is the reason that great majority of experimental investigations focused on the preparation and optimization of the g-CN1 photocatalysts for hydrogen production.

3.2 Electronic Properties of g-C₃N₄ 2D Structures

Because of intrinsic superiority of 2D structures and feasible exfoliation of the layered structures, many studies have been concentrated on the g-C₃N₄ nanosheets (g-CNSs) with atomic thickness and revealed remarkable success in improvement of the photoactivity. However, the effects of quantum size and surface states on electronic structures are usually ignored in most studies of the atomically ultrathin nanosheets. In our computations, electronic structures of g-CNSs with different thickness were computed. As listed in Table 1, the band gaps of g-CNSs vary

inversely with the thickness, owing to the size effect. g-CNSs with 4 atomic layers, corresponding to the thickness of 1–2 nm, have larger band gaps than the bulk structures to a small degree, implying a slight blue shift in comparison with the bulk g-C₃N₄.

It can be speculated that g-CNSs with proper thickness, maybe greater than 2 nm, should have band gaps and absorption spectra approaching those of bulk g-C₃N₄. Anyhow, the quantum size has evident effects on the electronic and optical properties of g-CNSs, which should never be neglected in the nanocrystallization of g-C₃N₄.

Table 1 Band gaps (in eV) of g-CN1 and g-CN2 nanosheets with different thickness, through HSE06 computations.

Geometry	g-CN1	g-CN2
1 Layer Nanosheet	3.03	3.81
2 Layer Nanosheet	2.85	3.51
3 Layer Nanosheet	2.79	3.42
4 Layer Nanosheet	2.75	3.38
Bulk	2.70	3.31

g-CNSs have such huge surface areas and so many dangling bonds on their surface, that the surface states should significantly affect their physicochemical properties. There are several kinds of inequivalently bonding N atoms in a primitive cell of bulk g-C₃N₄.⁵² Taking the g-CN1 for an example, as shown in Fig. 2a, there are two three-connected (N1 and N3) and six two-connected (N2) N atoms in a primitive cell. In consideration of the electron configuration (1s²2s²2p³) of N atoms, it is deemed that the three- and two-connected N atoms have two and three non-bonding electrons, respectively. Every C atom in g-CN1 is sp² hybridized and also has one non-bonding electron. Therefore, each C or N atom could attach to a hydrogen atom to form hydrogenated structures of g-C₃N₄. In fact, controllable and reversible protonation of g-CN1 was described by Wang et al in 2009.⁵³ It is widely accepted to date that g-CN1, which has primary building block of tri-s-triazine, is a more preferable photocatalyst. Due to its largest surface area, most surface dangling bonds and least number of atoms, the g-CN1 monolayer (g-CN1ML) may be the typical structure of the g-CN1 nanosheets. Accordingly, we only computed g-CN1MLs, as the representative of g-C₃N₄ nanosheets, for the following investigations. Geometric and electronic characteristics of the hydrogenated g-CN1 monolayer (H-g-CN1ML), with H adsorbing on different atoms, were calculated and listed in Table 2. Hydrogenation of N2 atoms in g-CN1ML has the lowest formation energy ($E_f = 0.08$ eV) and is the most energetically favourable, which may result from three non-bonding electrons in each N2 atom. Due to the saturation of surface states, all H-g-CN1MLs have larger band gaps than the bare g-CN1ML ($E_g = 3.03$ eV, Table 1), demonstrating the blue shift of light absorption. Hydrogenation of C1, C2, N1 and N2 atoms in H-g-CN1MLs should induce p-, p-, n-, and n-type semiconductors, respectively, which may result from the redistribution of electrons within the tri-s-triazine units. Additionally, the gap states in their band gaps imply the existence of charge recombination centers, which should also depress the photoactivity of g-CN1 nanosheets (see Fig. S1, Electronic Supplementary Information (ESI)). Therefore, the hydrogenated g-C₃N₄ nanosheet should be avoided in the design of 2D g-C₃N₄ photocatalysts, due to its blue-shift absorption and gap states in the band structure.

Table 2 Formation energies (E_f), band gaps (E_g) and defect levels of the g-CN1ML with different hydrogenated positions, through HSE06 computations.

Positions	E_f (in eV)	E_g (in eV)	Defect Levels
C1	1.38	3.71	Shallow
C2	1.35	3.85	Shallow
N1	2.09	3.74	Shallow
N2	0.08	4.10	Shallow
N3	1.55	3.97	Deep

3.3 Re-evaluation of Conventional Strategies for Improving the Photocatalytic Activity of g-C₃N₄ nanosheets

As mentioned above, 2D g-C₃N₄ materials have achieved in dramatically enhancing the photoactivity. However, as the results of the quantum size effect and saturation of surface dangling bonds, ultrathin g-CNSs may have larger band gaps, and thus, blue-shift light absorption. Many experimental and theoretical studies have succeeded in further reducing the band gaps and broadening the absorption spectrum of g-CNSs, through impurity doping, vacancy introducing, quantum dot loading and semiconductor coupling. To further select promising strategies for improving the photocatalytic performance of g-CNSs, we computed the geometric and electronic properties of modified g-CN1ML, which served as a typical example of g-CN1 nanosheets. After comparison and reliability test of the HSE06 and standard DFT (SDFT) method, we found that the SDFT with PBE functional can certainly predict the gap states and relative band width of g-CN1ML with N2 vacancy and N3-position hydrogenation (Fig. S2). Consequently, the SDFT method was employed for the computations of modified g-CN1MLs.

The formation energies of g-CN1ML with C/N vacancies and boron dopant were calculated according to the following formulas:⁵⁴

$$E_f(\text{Vacancy}) = E_T(\text{Vacancy}) - E_T(\text{Perfect}) + \mu_R, \quad \mu_R = \mu_C \text{ or } \mu_N \quad (4)$$

$$E_f(\text{Doped}) = E_T(\text{B-doped}) - [E_T(\text{Perfect}) + \mu_B - \mu_S], \quad \mu_S = \mu_C \text{ or } \mu_N \quad (5)$$

where $E_T(\text{Vacancy})$ and $E_T(\text{B-doped})$ are the total energies of g-CN1ML with C (or N) vacancies and C (or N) substituted by B, respectively, while the $E_T(\text{Perfect})$ is the total energy of the perfect g-CN1ML. μ_R is the chemical potential of the elements (C or N) removed from the g-CN1ML and μ_S is that of elements (C or N) substituted by B atoms. The beta rhombohedral B (R-3m: R group, 12 atoms in a unit cell), solid graphite (4 atoms in a unit cell) and gas N₂ are used to determine the chemical potentials: $\mu_B = \mu(\text{B}_{12})/12$, $\mu_C = \mu(\text{graphite})/4$ and $\mu_N = \mu(\text{N}_2)/2$. It is known that the larger band widths of CBM and VBM correspond to higher mobility of photo-induced electrons and holes, respectively, which is beneficial to rapid migration to the surface of photocatalysts before recombination.^{55–58} In our SDFT computations, the band widths of CBM (W_{CBM}) and VBM (W_{VBM}) are determined by the largest energy difference within the CBM and VBM band lines, respectively. For instance, the W_{CBM} and W_{VBM} of perfect g-CN1ML are calculated to be 0.56 eV and 0.32 eV, respectively (Fig. S3). Note that the PBE band gap of perfect g-CN1ML is 1.91 eV, which is the reference of the following discussion. For simplicity, the structures of g-CN1ML with vacancy, B dopant, CdSe-cluster loading and WTe₂ monolayer

coupling are tagged as V-g-CN1ML, B-g-CN1ML, CS-g-CN1ML and WT-g-CN1ML, respectively.

3.3.1 Vacancies in the g-CN1 nanosheets

Because of bonding with bridge N1 atoms, the removal of C1 leads to disconnection of the adjacent tri-s-triazine units and thus more serious distortion than the V-g-CN1MLs with C2 vacancy. Accordingly, the C1 removed g-CN1MLs have larger E_f than the C2 removed ones (see Table 3), implying energetic preferability of the latter. As well as the vacancies of C1, the absence of N1 should also result in this disconnection and severe lattice distortion. Therefore, g-CN1MLs with N1 vacancies have higher E_f than other N removed structures and should be energetically unfavourable. All the band gaps of V-g-CN1MLs are, more or less, smaller than that of the perfect g-CN1ML, in which the smallest band gap of C2 vacancy is 1.33 eV. The band widths of V-g-CN1ML are entirely smaller than those of g-CN1ML, denoting slower migration of photo-excited carriers within the former. Besides the C2 vacancy, introduction of vacancies results in gap states in the band structure of g-CN1MLs, denoting the presence of recombination centers and decline of photoactivity. Generally, it is suggested that the vacancies within the g-CN1 nanosheets should be refrained in photocatalysis, owing to the smaller band widths and recombination centers of excitons within V-g-CN1MLs. If unavoidable, the C2 vacancy in g-CN1 nanosheets is more preferable, owing to energetic favorability, no gap states and red-shift absorption of this structure.

Table 3 Formation energies (E_f , in eV), band gaps (E_g , in eV), defect levels, and CBM and VBM band widths (W_{CBM} and W_{VBM} , in eV) of g-CN1ML with vacancies in different positions, calculated by PBE functional.

Positions	E_f	E_g	Defect Levels	W_{CBM}/W_{VBM}
C1	1.83	1.88	Shallow	0.06/0.14
C2	1.12	1.33	No Gap State	0.12/0.03
N1	4.18	1.74	Deep	0.15/0.04
N2	1.95	1.80	Deep	0.11/0.02
N3	1.94	1.84	Deep	0.08/0.09

3.3.2 Improving the photoactivity through B doping

Table 4 Formation energies (E_f , in eV), band gaps (E_g , in eV), defect levels, and CBM and VBM band widths (W_{CBM} and W_{VBM} , in eV) of B-g-CN1ML with different positions of substitution, calculated by PBE functional.

Positions	E_f	E_g	Defect Levels	W_{CBM}/W_{VBM}
C1	-1.00	1.89	Shallow	0.24/0.06
C2	-0.87	1.82	Shallow	0.25/0.05
N1	1.34	1.03	No Gap State	0.13/0.05
N2	-0.33	0.90	No Gap State	0.15/0.06
N3	2.57	0.26	No Gap State	0.08/0.06

As listed in Table 4, the formation energies of the C1-, C2- and N2-position B doped g-CN1ML are negative, which suggests the spontaneous process of these substitutions. In contrary, the N1 and N3 substitution are thermodynamically unfavourable, which may result from the fewer outer electrons and smaller size of the B atoms. The exchange of B and N atoms in N1 or N3 position, results in the deficiency of electrons and lattice deformation in tri-s-triazine units. For example, the N3 substitution of B atoms, which is located in the center of tri-s-triazine, results in significant variation of the bond lengths and angles. The maximum difference between the bond lengths (angles) of C2-N3

(C2-N3-C2) and C2-B (C2-B-C2) is 0.14 Å (7.85°). B-g-CN1MLs with C substitution have gap states in their band structures and the band gaps approach those of g-CN1MLs, resulting in recombination center of carriers and similar light absorption to g-CN1ML. Band widths of the C substituted B-g-CN1MLs are smaller than those of g-CN1ML, especially the band widths of VBMs (see Table 4). This extremely smaller W_{VBM} should have detrimental effect on the migration of holes. As the results of gap states in band structures, extremely smaller band widths and similar light absorption spectrum to g-CN1ML, C substituted B-g-CN1MLs should be restrained and there would be no further discussion in the following sections.

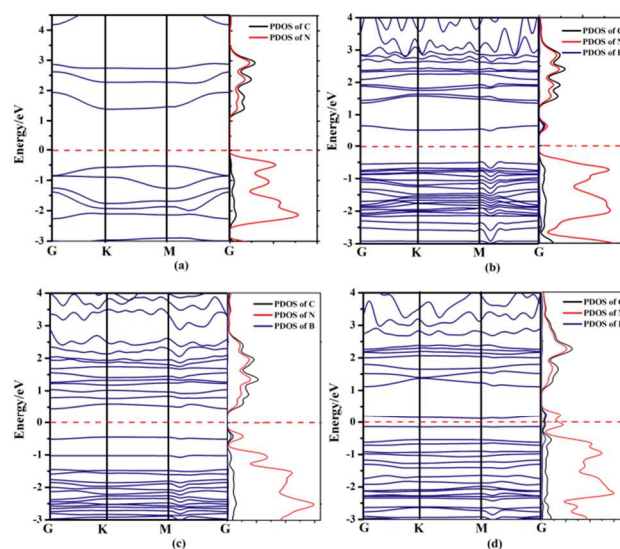


Fig. 6 Band structures and PDOS of (a) pure g-CN1ML, as well as (b) N1, (c) N2 and (d) N3 substituted B-g-CN1MLs. Red dashed lines present the Fermi level at 0 eV.

All the N substituted g-CN1MLs have notably smaller band gaps and band widths than the perfect ones, which results in the red-shift absorption but decreased carrier mobility of the former. Fortunately, substitution of N should not induce gap states. Considering the remarkably red shift of light absorption, band structures and partial density of states (PDOS) of these N substituted B-g-CN1MLs, as well as those of pure g-CN1ML, are presented in Fig. 6. As shown in Fig. 6b, we found evidently splitting of the conduction band in band structures of the N1 substituted B-g-CN1ML, which results in relatively descending of the CBM levels, and thus, decreased band gaps. For N1 substituted B-g-CN1ML, splitting of the conduction band is further confirmed by the isolated peak below the primary conduction band of g-CN1ML, as shown in the PDOS of Fig. 6b. Similarly, the N2 substitution in B-g-CN1ML leads to the split valence band and raised VBM levels (Fig. 6c). Both the conduction band and valence band are obviously split in band structure of N3 substituted B-g-CN1ML, which leads to greater reduction of their band gaps (Fig. 6d). Except for the decreased carrier mobility, which may be overcome by the distance of several nanometers of during the exciton migration to the surface of these ultrathin nanostructures, N substitution of B-g-CN1ML may be a promising strategy for promoting the photoactivity of g-CN1MLs. However, the excessive reduction of band gap within N3 substituted B-g-CN1ML may lead to severe diminishing

energy difference between the CBM (or VBM) levels and $\phi(\text{H}^+/\text{H}_2)$ [or $\phi(\text{O}_2/\text{H}_2\text{O})$], and thus, incapability of water-splitting.

3.3.3 Synergistic effects within the CdSe cluster loading and WTe₂ coupling g-CN1 nanosheets.

As ideal choices for improving the photoactivity, structural and electronic properties of quantum dot loading and semiconductor coupling g-CN1MLs were also calculated in our study. Formation energies of these modified g-CN1MLs are determined by the following equation:

$$E_f(\text{m-g-CN1ML}) = E_f(\text{m-g-CN1ML}) - [E_f(\text{g-CN1ML}) + E_f(x)] \quad (6)$$

where $E_f(\text{m-g-CN1ML})$ is the formation energy of the CdSe cluster or WTe₂ monolayer modified g-CN1ML, $E_f(\text{m-g-CN1ML})$ and $E_f(\text{g-CN1ML})$ are total energies of modified and pure g-CN1MLs, respectively. $E_f(x)$ presents the energy of CdSe cluster or WTe₂ monolayer.

Table 5 Formation energies (E_f), band gaps (E_g), and CBM and VBM band widths of the CS-g-CN1ML and WT-g-CN1ML, computed by PBE functional.

Structures	E_f (in eV)	E_g (in eV)	$W_{\text{CBM}}/W_{\text{VBM}}$ (in eV)
CS-g-CN1ML	0.13	1.53	0.07/0
WT-g-CN1ML	0.11	0.73	0.70/0.51

As listed in Table 5, both CS-g-CN1ML and WT-g-CN1ML have formation energies around 0.10 eV, which may indicate the thermodynamic stability and possible synthesis of these structures. The band gaps of these modified g-CN1MLs are smaller than that of the isolated one and there is no gap state in the band structures of CdSe quantum dot loaded or WTe₂ coupled g-CN1MLs (as shown in Fig. 7). The CBM and VBM band widths of the WT-g-CN1ML are 0.70 eV and 0.51 eV, which are greater than those of unmodified g-CN1ML ($W_{\text{CBM}} = 0.56$ eV and $W_{\text{VBM}} = 0.32$ eV), respectively, implying higher mobility of electrons and holes within WTe₂ coupled g-CN1ML. However, the approximately flat CBM and VBM band lines of CS-g-CN1ML suggests near zero mobility and localized carriers within the CdSe cluster loaded g-CN1ML, which is unfavourable in the photocatalysis (see Table 5 and Fig. 7). Reduction of band gaps is further confirmed by the PDOS of CS-g-CN1ML and WT-g-CN1ML. As shown in Fig. 7, the CBMs and VBMs of these modified g-CN1MLs are contributed by g-CN1 and WTe₂ (or CdSe) components of the WT-g-CN1ML (or CS-g-CN1ML) nanosheets, respectively, which belong to the type-II band offset in heterostructured semiconductors. It has been found in our recent work³⁸ that the type-II band alignment of constituents in coupled semiconductors leads to the evidently decreased band gaps and directly separated carriers within these structures. The spatial distributions of CBMs and VBMs at the Γ point are also computed for these modified g-CN1MLs, which is in agreement with the PDOS, as shown in Fig. S4. In other words, the photo-induced electrons and holes within the photo-excited WT-g-CN1ML (CS-g-CN1ML) are directly separated and spatially confined in the g-CN1 and WTe₂ (CdSe) regions, respectively.

According to the synergism between g-CN1 and WTe₂ (or CdSe), the modified g-CN1MLs have evidently red-shift light absorption, absent gap states, as well as direct separation and spatial confinement of photo-excited electrons and holes in these structures, which is favourable in photocatalytic reactions. The

band widths of CBM and VBM changed obviously, which may be also due to the synergistic effects of g-CN1 and WTe₂ (or CdSe) components. The higher W_{CBM} and W_{VBM} of WT-g-CN1ML suggest the greater mobility of photo-induced electrons and holes in it, respectively, implying the superiority of these kinds of cooperation. As a result of quantum size effect, the photo-excited CdSe quantum dot has localized carriers with low mobility and spatial distribution in its own region. In contrary, 2D extending structure of the WTe₂ monolayer results in delocalization of the photo-induced charges, exhibiting the rapid migration of excitons. In general, both the WTe₂ coupled and CdSe cluster loaded g-CN1 nanosheets are promising photocatalysts, and the WTe₂ coupled g-CN1 nanosheet is preferable in photocatalysis, owing to its extraordinary characters including broadened light absorption, directly separated and spatially confined carriers, as well as rapid migration of photo-excited carriers.

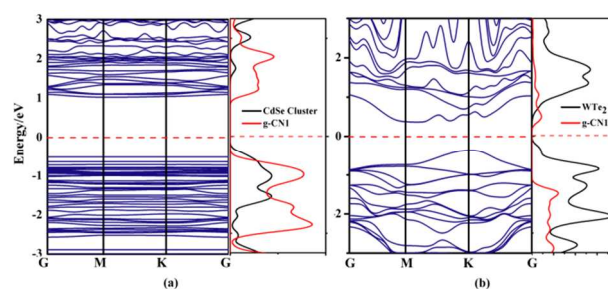


Fig. 7 Band structures and PDOSs of the (a) CS-g-CN1ML and (b) WT-g-CN1ML.

4. Conclusions

In conclusion, we have investigated the origin of graphitic carbon nitrides' photocatalytic activity and compared the conventional strategies for promoting the photoactivities of g-C₃N₄, through first-principles computations. The bulk g-CN1, which consists of tri-*s*-triazine units, has visible-light absorption, proper band edge potentials, and indirect band gaps, implying the favorability of it in the photocatalysis. Although 2D nanocrystallization of g-CN1 is beneficial to the improvement of its photocatalytic activities, 2D g-CN1 nanosheets need to overcome the effects of quantum size and surface states on its band structures. Excessive minimization and surface hydrogenation should be avoided in pure g-CN1 nanosheets, as the result of its dramatically increased band gaps caused by nanocrystallization and surface passivation.

Additionally, introduction of vacancies results in gap states and smaller band widths, which should be restrained in the g-CN1 nanosheets. If unavoidable, C2-position vacancy is preferable, owing to the decreased band gaps and absent gap states in its band structure. C substituted B-g-CN1MLs should also be inhibited, due to the existence of gap states and extremely smaller band widths. N substitution may be favourable for enhancing the photoactivities of g-CN1, thanks to the red-shift light absorption and free gap states within this B doped g-CN1 nanosheets.

The synergistic effect between the g-CN1 nanosheets and other nanostructured semiconductors, such as WTe₂ monolayer or CdSe quantum dot, leads to the decreased band gaps and direct

separation of photo-excited carriers in the modified g-CN1MLs, which is beneficial to improve the photoactivities of g-CN1. Compared with the load of CdSe cluster, the WTe₂ coupled g-CN1 nanosheets are more favourable for the promotion of photoactivities, due to the more rapidly migrating excitons.

Acknowledgement

This work was supported by Anhui Provincial Department for Scientific Research of College and Universities (KJ2013A018), Start-up Funds for Doctors of Anhui University, NSFC (21273118 and 21403001) and MOE Innovation Team (IRT13R30) in China.

^a Anhui Key Laboratory of Information Materials and Devices, School of Physics and Materials Science, Anhui University, Hefei 230601, P. R. China. E-mail: liguang1971@ahu.edu.cn

^b Tianjin Key Laboratory of Metal and Molecule Based Material Chemistry, Key Laboratory of Advanced Energy Materials Chemistry (Ministry of Education), Computational Centre for Molecular Science, Institute of New Energy Material Chemistry, Collaborative Innovation Center of Chemical Science and Engineering (Tianjin), Nankai University, Tianjin 300071, P. R. China. E-mail: zhouzhen@nankai.edu.cn

Notes and references

- 1 X. Wang, K. Maeda, A. Thomas, K. Takanabe, G. Xin, J. M. Carlsson, K. Domen and M. Antonietti, *Nat. Mater.*, 2009, **8**, 76.
- 2 J. Zhang, X. Che, K. Takanabe, K. Maeda, K. Domen, J. D. Epping, X. Fu, M. Antonietti and X. Wang, *Angew. Chem. Int. Ed.*, 2010, **49**, 441.
- 3 Y. Wang, X. Wang and M. Antonietti, *Angew. Chem. Int. Ed.*, 2012, **51**, 68.
- 4 P. Niu, L. Zhang, G. Liu and H. Cheng, *Adv. Funct. Mater.*, 2012, **22**, 4763.
- 5 H. Zhao, H. Yu, S. Chen, Y. zhang, H. Zhao and H. Wang, *Appl. Catal. B: Environ.*, 2014, **152**, 46.
- 6 B. Yuan, Z. Chu, G. Li, Z. Jiang, T. Hu, Q. Wang and C. Wang, *J. Mater. Chem. C*, 2014, **2**, 8212.
- 7 X. Zhang, X. Xie, H. Wang, J. Zhang, B. Pan and Y. Xie, *J. Am. Chem. Soc.*, 2013, **135**, 18.
- 8 K. Schwinghammer, M. B. Mesch, V. Duppel, C. Ziegler, J. Senker and B. V. Lotsch, *J. Am. Chem. Soc.*, 2014, **136**, 1730.
- 9 S. Bai, X. Wang, C. Hu, M. Xie, J. Jiang and Y. Xiong, *Chem. Commun.*, 2014, **50**, 6094.
- 10 X. Wang, X. Chen, A. Thomas, X. Fu and M. Antonietti, *Adv. Mater.*, 2009, **21**, 1609.
- 11 G. Dong, K. Zhao and L. Zhang, *Chem. Commun.*, 2012, **48**, 6178.
- 12 X. Ma, Y. Lv, J. Xu, Y. Liu, R. Zhang and Y. Zhu, *J. Phys. Chem. C*, 2012, **116**, 23485.
- 13 J. Hong, X. Jia, Y. Wang and R. Xu, *J. Mater. Chem.*, 2012, **22**, 15006.
- 14 J. A. Singh, S. H. Overbury, N. J. Dudney, M. Li and G. M. Veith, *ACS Catal.*, 2012, **2**, 1138.
- 15 L. Ge, F. Zuo, J. Liu, Q. Ma, C. Wang, D. Sun, L. Bartels and P. Feng, *J. Phys. Chem. C*, 2012, **116**, 13708.
- 16 N. Chen, J. Tian, Q. Liu, C. Ge, A. H. Qusti, A. M. Asiri, A. Al-Youbi and X. Sun, *ACS Appl. Mater. Interfaces*, 2013, **5**, 6815.
- 17 J. Yu, K. Wang, W. Xiao and B. Chen, *Phys. Chem. Chem. Phys.*, 2014, **16**, 11492.
- 18 S. Min and G. Lu, *J. Phys. Chem. C*, 2012, **116**, 19644.
- 19 Y. Wang, X. Bai, C. Pan, J. He and Y. Zhu, *J. Mater. Chem.*, 2012, **22**, 11568.
- 20 C. Pan, J. Xu, Y. Wang, D. Li and Y. Zhu, *Adv. Funct. Mater.*, 2012, **22**, 1518.
- 21 Y. Wang, Z. Wang, S. Muhammad and J. He, *CrystEngComm*, 2012, **14**, 5065.
- 22 J. Sun, Y. Yuan, L. Qiu, X. Jiang, A. Xie, Y. Shen and J. Zhu, *Dalton Trans.*, 2012, **41**, 6756.
- 23 L. Sun, X. Zhao, C. Jia, Y. Zhou, X. Cheng, P. Li, L. Liu and W. Fan, *J. Mater. Chem.*, 2012, **22**, 23428.
- 24 W. Wang, J. Yu, D. Xia, P. K. Wong and Y. Li, *Environ. Sci. Technol.*, 2013, **47**, 8724.
- 25 L. Shi, L. Liang, J. Ma, F. Wang and J. Sun, *Dalton Trans.*, 2014, **43**, 7236.
- 26 Y. Zhu, M. Li, Y. Liu, T. Ren and Z. Yuan, *J. Phys. Chem. C*, 2014, **118**, 10963.
- 27 Q. Deng, L. Liu, X. Lin, G. Du, Y. Liu and Z. Yuan, *Chem. Eng. J.*, 2012, **203**, 63.
- 28 H. Pan, Y. Zhang, V. B. Shenoy and H. Gao, *ACS Catal.*, 2011, **1**, 99.
- 29 F. Wu, Y. Liu, G. Yu, D. Shen, Y. Wang and E. Kan, *J. Phys. Chem. Lett.*, 2012, **3**, 3330.
- 30 J. Xu, Y. Wang and Y. Zhu, *Langmuir*, 2013, **29**, 10566.
- 31 P. E. Blöchl, *Phys. Rev. B*, 1994, **50**, 17953.
- 32 G. Kresse and D. Joubert, *Phys. Rev. B*, 1999, **59**, 1758.
- 33 G. Kresse and J. Hafner, *Phys. Rev. B*, 1994, **49**, 14251.
- 34 J. P. Perdew, K. Burke and M. Ernzerhof, *Phys. Rev. Lett.*, 1996, **77**, 3865.
- 35 J. Heyd, G. E. Scuseria and M. Ernzerhof, *J. Chem. Phys.*, 2006, **27**, 1787.
- 36 S. Saha, T. P. Sinha and A. Mookerjee, *Phys. Rev. B*, 2000, **62**, 8828.
- 37 S. Grimme, *J. Comput. Chem.*, 2006, **27**, 1787.
- 38 H. Zhang, D. Wu, Q. Tang, L. Liu and Z. Zhou, *J. Mater. Chem. A*, 2013, **1**, 2231.
- 39 M. Gajdoš, K. Hummer, G. Kresse, J. Furthmüller and F. Bechstedt, *Phys. Rev. B*, 2006, **73**, 045112.
- 40 S. Chen and L. Wang, *Chem. Mater.*, 2012, **24**, 3659.
- 41 H. Tong, S. Ouyang, Y. Bi, N. Umezawa, M. Oshikiri and J. Ye, *Adv. Mater.*, 2012, **24**, 229.
- 42 S. Wei and A. Zunger, *Phys. Rev. Lett.*, 1987, **59**, 144.
- 43 S. Wei and A. Zunger, *Appl. Phys. Lett.*, 1998, **72**, 2011.
- 44 S. Chen, J. Yang, X. Gong, A. Walsh and S. Wei, *Phys. Rev. B*, 2010, **81**, 245204.
- 45 H. Zhuang and R. G. Henning, *J. Phys. Chem. C*, 2013, **117**, 20440.
- 46 G. L. Gutsev, E. Johnson, M. D. Mochena and C. W. Bauschlicher, *J. Chem. Phys.*, 2008, **128**, 144707.
- 47 K. A. Nguyen, R. Pachter and P. N. Day, *J. Chem. Theory Comput.*, 2013, **9**, 3581.
- 48 M. Deifallah, P. E. McMillan and F. Corà, *J. Phys. Chem. C*, 2008, **112**, 5447.
- 49 L. Alves, G. Demazeau, B. Tanguy and F. Weill, *Solid State Commun.*, 1999, **109**, 697.
- 50 V. N. Khabashesku, J. L. Zimmerman and J. L. Margrave, *Chem. Mater.*, 2000, **12**, 3264.
- 51 A. H. Reshak, S. A. Khan and S. Auluck, *RSC Adv.*, 2014, **4**, 6957.
- 52 H. Qiu, Z. Wang and X. Sheng, *Physica B: Condensed Matter.*, 2013, **421**, 46.
- 53 Y. Zhang, A. Thomas, M. Antonietti and X. Wang, *J. Am. Chem. Soc.*, 2009, **131**, 50.
- 54 K. Yang, Y. Dai and B. Huang, *J. Phys. Chem. C*, 2007, **111**, 18985.
- 55 W. Huang, *J. Comput. Chem.*, 2009, **30**, 1882.
- 56 H. Zhang, L. Liu and Z. Zhou, *Phys. Chem. Chem. Phys.*, 2012, **14**, 1286.
- 57 H. Zhang, L. Liu and Z. Zhou, *RSC Adv.*, 2012, **2**, 9224.
- 58 H. Zhang, Y. Yang, Z. Zhou, Y. Zhao and L. Liu, *J. Phys. Chem. C*, 2014, **118**, 14662.